The original publication is available at http://dx.doi.org/10.1115/1.4037749

Detailed Examination of a Modified Two-Stage Micro Gas Turbine Combustor

Andreas Schwärzle*

German Aerospace Center (DLR)
Institute of Combustion Technology
Pfaffenwaldring 38-40
70569 Stuttgart, Germany
Email: andreas.schwaerzle@dlr.de

Thomas O. Monz

German Aerospace Center (DLR)
Institute of Combustion Technology
Pfaffenwaldring 38-40
70569 Stuttgart, Germany

Andreas Huber
Manfred Aigner

German Aerospace Center (DLR)
Institute of Combustion Technology
Pfaffenwaldring 38-40
70569 Stuttgart, Germany

ABSTRACT

Jet-stabilized combustion is a promising technology for fuel flexible, reliable, highly efficient combustion systems. The aim of this work is a reduction of NO_x emissions of a previously published two-staged MGT combustor [1, 2], where the pilot stage of the combustor was identified as the main contributor to NO_x emissions. The geometry optimization was carried out regarding the shape of the pilot dome and the interface between pilot and main stage in order to prevent the formation of high temperature recirculation zones. Both stages have been run separately to allow a detailed understanding of the flame stabilization within the combustor, its range of stable combustion, the interaction between both stages and the influence of the modified geometry. All experiments were conducted at atmospheric pressure and an air preheat temperature of 650 °C. The flame was analyzed in terms of shape, length and lift-off height, using OH^* chemiluminescence images. Emission measurements for NO_x, CO and UHC emissions were carried out. At a global air number of $\lambda = 2$, a fuel split variation was carried out from 0 (only pilot-stage) to 1 (only main stage). The modification of the geometry lead to a decrease in NO_x and CO emissions throughout the fuel split variation in comparison with the previous design. Regarding CO emissions, the pilot stage operations is beneficial for a fuel split above 0.8. The local maximum in NO_x emissions observed for the previous combustor design at a fuel split of 0.78 was not apparent for the modified design. NO_x emissions were increasing, when the local air number of the pilot stage was below the global air number. In order to evaluate the influence of the modified design on the flow field and identify the origin of the emission reduction compared to the previous design, unsteady RANS simulations were carried out for both geometries at fuel splits of 0.93 and 0.78, respectively, using the DLR in-house code THETA with the k-w SST turbulence model and the DRM22 [3] detailed reaction mechanism. The numerical results showed a strong influence of the recirculation zones on the pilot stage reaction zone.

Nomenclature

Latin Letters

*Address all correspondence to this author.

a, b, c, d, e	location a, b, c, d, e
C	Emission concentration (Vol. % or ppm)
$\dot{m}$	Mass flow rate (g/s)
S	Mass flow split between main and pilot stage
u, v, w	velocity in x-, y-, z-direction
$y+$	dimensionless wall distance

Greek Letters

λ	Air number (-)
θ	Circumferential velocity, yz-Plane (m/s)

Subscripts

amb	ambient
corr	corrected
exp	experiment
f	fuel
g	global
m	main
meas	measured
p	pilot
pre	preheat
recirc	recirculated
ref	reference
rel	relative
sim	simulation

Abbreviations

$\dot{Q}$	Thermal Power (kW)
R	Recirculation rate (-)
FL	Flame Length (mm)
HAB	Height Above Burner (mm)
IRZ	Inner Recirculation Zone
LBO	Lean Blowout
LHV	Lower Heating Value (MJ/kg)
MGT	Micro Gas Turbine
MS	Main Stage
OH-CL	OH^* chemiluminescence
ORZ	Outer Recirculation Zone
PRZ	Primary Reaction Zone
PS	Pilot Stage

1 Introduction

With a further increase in world population and people's pursuit for convenience and wealth, the world energy demand is ever increasing [4]. One of engineers major task is to address this energy hunger by increasing efficiency and reducing emissions, so that the world's use of primary energy can still be reduced. Expanding the use of decentralized energy systems is one piece in the puzzle to achieve this. Although electric efficiency may not be as high as in large combined cycle gas turbines (CCGT), decentralized micro gas turbine (MGT) based combined heat and power (CHP) generation can persist due to negligible losses in heat and power transmission.

At the DLR Institute for Combustion, a jet-stabilized combustor was developed for the Turbec T100, 100 kW_{el} class micro gas turbine [5, 6]. The advantage of a jet-stabilized combustion are low emissions [7, 8, 9], fuel flexibility and the capability to handle high H2-content gases without the risk of flashback [10]. In order to operate the combustor from a cold start up to full load MGT conditions, a swirl stabilized pilot stage was developed and incorporated in the combustor design [1]. Figure 1 shows a schematic of a jet-stabilized MGT combustor with a stabilizing swirl pilot stage. The primary combustion zone is characterized by a large inner recirculation zone, driven by the high momentum jets of the main stage. Before the combustion chamber exit, the hot exhaust gases are diluted in order to meet the temperature restrictions imposed by the turbine material. Since the targeted single digit emission values for full load conditions could not be achieved during MGT experiments. A detailed examination of the combustor was carried out by Schwärzle et al. [2] that identified the swirl pilot stage as main contributor to NO_x emissions.

The original publication is available at http://dx.doi.org/10.1115/1.4037749

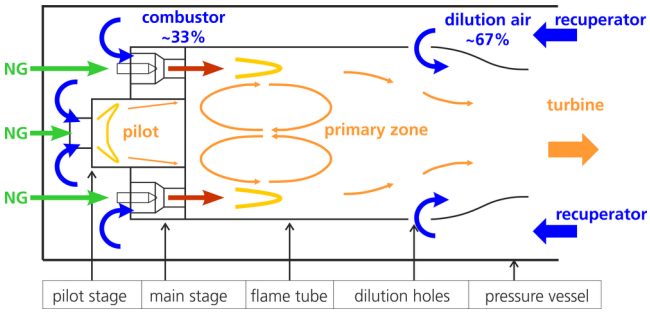

Fig. 1: Schematic of a jet-stabilized MGT combustor including mixing air holes (dilution) and flow path. About 33 % of the air is fed to the pilot and the main stage of the combustor. The larger amount of air is used for dilution.

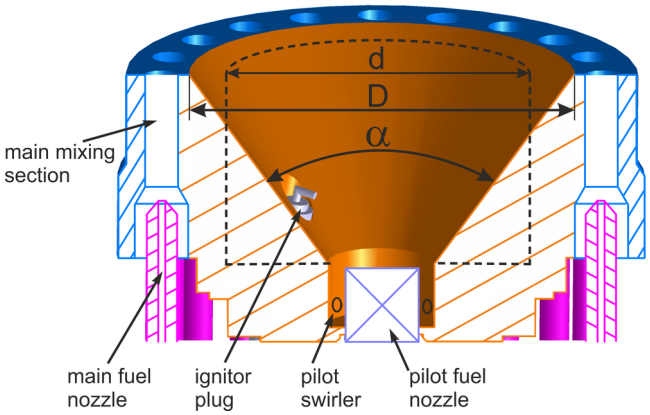

Fig. 2: Modified version of the two-staged combustor with a 20 nozzle jet-stabilized main stage (blue) and a 10 nozzle swirl-stabilized pilot stage (orange). The dashed line indicates the shape of the original pilot stage.

Combustor Modification

The modification carried out on the original combustor, from now on termed as *standard* combustor, refers to the shape of the pilot dome. Here, a cone like shape was introduced instead of the cylindrical shape of the standard combustor, following the basic idea of removing the outer recirculation zone (ORZ) within the pilot stage and feeding the hot exhaust gases from the pilot stage more easily to the main stage nozzles. This is also supported by an increased exit diameter of the pilot dome. The modified combustor will be termed as *cone* combustor due to its characteristic shape.

Figure 2 shows a section of the modified combustor design. The main stage of the combustor consists of twenty annular nozzles. The fuel and air of the main stage is technically premixed in the main mixing section before entering the primary combustion zone. The pilot stage is located in the center of the combustor and is recessed with respect to the main stage outlet surface. The cylindrical shape of the pilot stage of the standard combustor with the diameter d is indicated by a dashed line. The cone combustor has a larger exit diameter D and a cone shaped dome with the opening angle α. No changes were made to the pilot swirler, consisting of ten air nozzles, and the centered pilot fuel nozzle.

The flow field within the atmospheric test rig for both combustors is seen in Fig. 3, with the standard and the cone combustor shown on top and bottom, respectively. The simulation shows the reactive flow field at an air mass flow rate of $\dot{m}_{air} = 60$ g/s, a global air number of $\lambda_g = 2.0$ and a fuel split of $S_f = 0.93$ at a preheat temperature of 650 °C. The numerical setup and the boundary conditions are given later in this paper. Characteristic for the combustors is the large inner recirculation zone (IRZ). Here, the hot exhaust gases are recirculated and mixed with the fresh fuel air mixture from the pilot and the main stage. The area of the IRZ is extended further downstream for the cone combustor. Within the pilot dome, the IRZ reaches its upstream limit at the pilot fuel nozzle. The ORZ is only present for the standard combustor. The small recirculation zone at the 90 degree flow redirection of the pilot exhaust at the standard combustor is avoided for the cone combustor due to the increased exit diameter and wide opening angle of the pilot dome.

Experimental and Numerical Setup

The atmopheric combustor test rig is shown in Fig. 4. The preheated air is supplied at location ⓐ. Following the flow path, indicated by the dashed arrows, the air is redirected around the yellow baffle, which is needed to reproduce the flow path

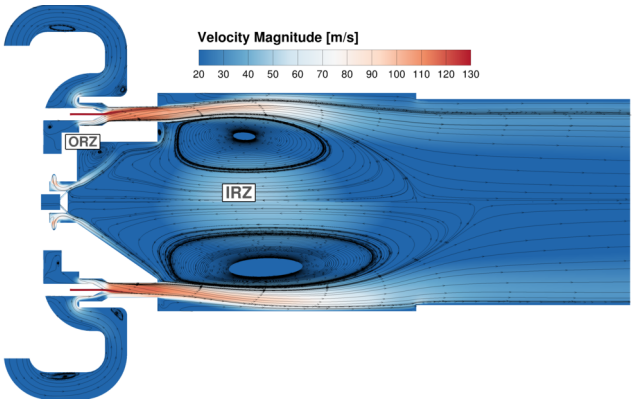

Fig. 3: CFD simulation of the standard (top) and cone (bottom) combustor in the atmospheric test rig at $\dot{m}_{air} = 60$ g/s a fuel split of $S_f = 0.93$ and 650 °C, showing the averaged absolute velocity including streamline patterns.

within the Turbec T100 MGT, where the flow is redirected by 180 degree. The flow conditioner at location ⓑ corresponds to the inlet boundary, while the exit plane of the test rig ⓔ corresponds to the outlet boundary of the simulated domain. At location ⓒ, the preheat temperature and the inlet pressure is measured. This is also the reference position for the numerical simulation, where the reference pressure is defined. The exhaust gas probe is located in the center of the test rig, close to the exit plane at location ⓓ.

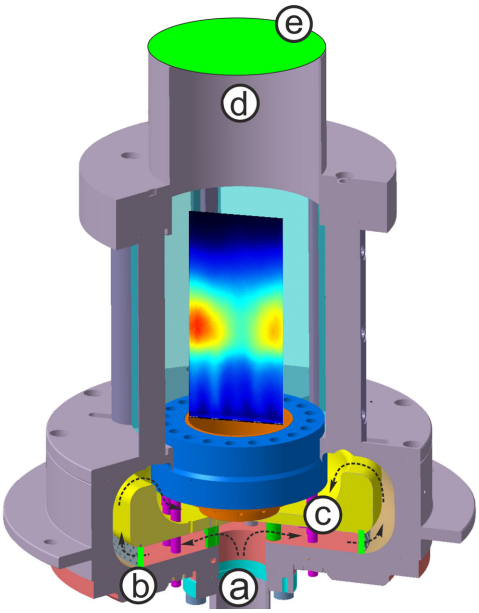

Fig. 4: Atmospheric combustor test rig with exemplary OH* chemiluminescence image including air flow path (dashed arrows) and baffle (yellow) [2]. ⓐ – air inlet, ⓑ – Simulation: Air inlet, ⓒ – location of static pressure and preheat temperature gauges in combustor plenum, ⓓ – location of exhaust gas probe for emission measurements, ⓔ – Simulation: Outlet.

The air split between the pilot stage and the main stage can be calculated from the static combustor inlet pressure and the preheat temperature from a map that was created during the calibration procedure performed on the standard combustor. Since the modification of the combustor only concerns the downstream side and not the inflow area or air plenum, the validity of the calibration procedure persists for the cone combustor. The global, main and pilot air number is calculated using Eqn. (1)

$$\lambda = \frac{\dot{m}_{air}}{\dot{m}_f \cdot AFR}, \tag{1}$$

the air split, the respective fuel mass flow rates and the air fuel ratio (AFR – air fuel ratio, $\dot{m}$ – mass flow rate). The static combustor pressure loss is calculated from the static combustor inlet pressure p_c and the ambient pressure p_{amb} using Eqn. (2)

$$\Delta p_{rel} = \frac{p_c - p_{amb}}{p_c} \cdot 100\,\%. \tag{2}$$

Design of Experiment

All experiments were carried out at atmospheric pressure conditions and a combustor inlet temperature of 650 °C. Four sets of experiments were carried out. In two sets of experiments, the main and pilot stage are operated separately by reducing the fuel mass flow rate of the respective stage from an initial global air number of λ_g = 2.0, leaving the air mass flow rate at $m_{air} = 60\,g/s$. The interaction between both stages is examined during a fuel split variation. The fuel split is calculated using Eqn. (3)

$$S_f = \frac{\dot{m}_{f,m}}{\dot{m}_{f,m} + \dot{m}_{f,p}}, \tag{3}$$

where the fuel mass flow rate of the main stage is divided by the total fuel mass flow rate. The fuel split is varied from 0 (only pilot stage) to 1 (only main stage) at a constant global air number of λ_g = 2.0 and air mass flow rate at $\dot{m}_{air} = 60\,g/s$. In addition a variation in air mass flow rate is carried out at a thermal power input of $\dot{Q}$ = 100 kW. This allows the identification of the optimum air split between combustion and dilution air. All experiments are summarized in Tab. 1, where the constant value (CONST) as well as the variable (VAR) minimum and maximum are given.

The natural gas for the experiments on the cone combustor had a typical composition (per volume) of CH_4: 94.17 – 94.47 %, C_2H_6: 3.45 – 3.57 %, higher hydrocarbons: 0.41 – 0.44 %, inert species: 1.66 – 1.84 % and $H_2 < 0.004$ %. The heating value and the air fuel ratio are calculated from the average composition. This corresponds to a lower heating value of LHV = 47.91 – 48.10 MJ/kg and an air fuel ratio of AFR = 16.49–16.55. The natural gas composition during the experiments with the standard combustor can be found in [2].

Table 1: Design of the four sets of experiments showing the value kept constant (CONST) and the minimum and maximum of the varied values (VAR).

#	Descr.	CONST	VAR	VAR min	VAR max
1	pilot	$\dot{m}_{air} = 60\,\frac{g}{s}$	λ $\dot{m}_f$	$\lambda_p = 0.14$	$\lambda_p = 1.2$
2	main	$\dot{m}_{air} = 60\,\frac{g}{s}$	λ $\dot{m}_f$	$\lambda_m = 1.86$	$\lambda_m = 3.63$
3	split	$\dot{m}_{air} = 60\,\frac{g}{s}$ $\lambda_g = 2.0$	S_f	$S_f = 0$	$S_f = 1$
4	$\dot{Q}$ = 100 kW	$\dot{Q} = 100$ kW $S_f = 0.93$	λ_g $\dot{m}_{air}$	$\lambda_g = 1.6$ $\dot{m}_{air} = 55\,\frac{g}{s}$	$\lambda_g = 3.4$ $\dot{m}_{air} = 117\,\frac{g}{s}$

Optical Measurements

The flame was analyzed using a LaVision ICCD camera provided with appropriate filters (see [2]) to detect the signal from the OH^* molecule. An exemplary OH^* chemiluminescence (OH-CL) image is shown in Fig. 4. Since the OH^* molecule is formed in areas of highest heat release rates mostly through the $CH + O_2 \rightleftharpoons CO + OH^*$ reaction (for methane air flames) [11], it is a good marker for the position of the flame front. OH-CL is a line of sight technique. Therefore, the signal is integrated over the volume of the combustion chamber (Fig. 5a), showing four main stage nozzles. Because of limitations in the build-up of the test rig, the combustor is rotated by one angular degree. A series of 500 instantaneous images were recorded at a rate of 8 Hz. Figure 5b shows the step from the corrected OH-CL image to the area of the flame. In addition it shows the definition of the height above the burner (HAB) or lift-off height and the flame length (FL) defined in [6, 2].

Emission Measurements

For the exhaust gas analysis of the combustor the combustion exhaust is extracted via an air cooled gas probe. This allows a rapid cooling of the extracted gas in order to freeze its current composition. The ABB process gas analyzer is able

The original publication is available at http://dx.doi.org/10.1115/1.4037749

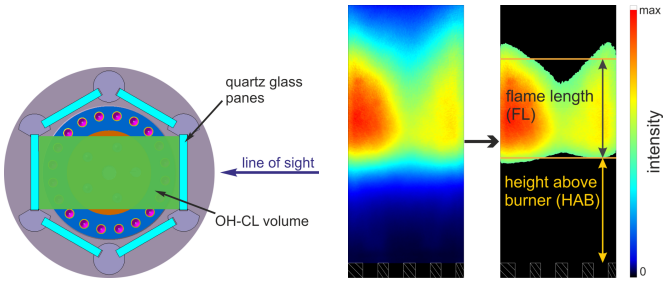

(a) (b)

Fig. 5: Volume for OH* imaging, seen by the ICCD camera (a) and definition of the height above the burner (HAB) and the flame length (FL) for an OH* image (b) [2].

to detect O_2, the combustion products H_2O and CO_2 as well as the pollutants CO, NO, NO_2 and unburned hydro carbons (UHC). The accuracies of the analyzers is given in [2]. While O_2, CO and CO_2 are detected in the dry exhaust gas, the other species are measured in wet conditions. Unless stated otherwise, all emissions are given on a dry basis and normalized to 15 % oxygen content, based on Eqn. (4)

$$C_{corr} = C_{meas} \cdot \frac{21 - 15}{21 - C_{O_2}[Vol.\%]}, \tag{4}$$

as stated in the TA-Luft [12]. C_{meas} and C_{corr} are the measured and the corrected emissions, respectively. C_{O_2} is the measured oxygen content in the exhaust gas given in percent volume. All emissions are normalized to the emissions of a reference point. Since no UHC emissions were measured at $\lambda_g < 2.0$, these emissions are normalized by the CO emissions of the reference point. The reference point for experiment 1-3 (see Tab. 1) is $\lambda_g = \lambda_m = 2.0$ (main stage only operation) and $\dot{m}_{air}$ = 60 g/s, while for experiment 4 it is $\lambda_g = 2.0$ and $S_f = 0.93$. All measurements were recorded at a rate of 2 Hz and were time-averaged for at least 3 min.

Numerical Simulation

The simulation was carried out using the incompressible DLR in-house combustion CFD code THETA [13] (**T**urbulent **H**eat Release **E**xtension of the **TA**U code) with the strain rate formulation of the k-ω-SST turbulence model by Menter et al. [14]. For combustion modeling, a stiff chemical solver with a finite rate chemistry model is used. The turbulence chemistry interaction (TCI) is realized using an assumed-PDF approach [15] for temperature (Gauss distributed) and species (multivariate β-PDF [16]). The DRM22 [3] reaction mechanism was used, which is a reduced version of the GRI-1.2 mechansim [17] that consists of 22 reacting species (+2 inert) and 104 reactions.

The simulated domain comprises 36 degree of the test rig geometry and contains ∼460 000 points for the standard (Fig. 6a) and ∼500 000 points for the cone combustor (Fig. 6b). The main mixing nozzles as well as the primary reaction area is meshed using sweep functions in order adjust the orientation of the mesh to the main flow direction within the primary reaction zone. In order to resolve the flow in the boundary layer or wall near region, ten prism layers are introduced. The resulting near wall resolvement is for 65 % of the cells $y+ < 1$ for 35 % of the cells $1 < y+ < 5$ and for 2 % of the cells that are located upstream of the combustor $y+ > 5$.

Simulations were carried out as reactive and non-reactive URANS for both combustor geometries at fuel splits of S_f = 0.93 and 0.78. The time step size was 5e-7 s per iteration. All results shown are time averaged over at least 0.02 s. Instead of the natural gas composition from the experiment, only methane was used as fuel with a fuel mass flow rate of $\dot{m}_{f,tot}$ = 1.74 g/s for the full geometry.

Results

The standard two-staged jet-stabilized combustor has been experimentally characterized in detail by Zanger and Schwärzle [1, 18, 2]. Here, the results on the combustor modification are shown and a comparison to the standard combustor is carried out. The numerical results are adduced for a better understanding of the experimental results. They give valuable insights in the three dimensional flow field, turbulent quantities and species distribution. During the experiments, no combustion instabilities were apparent.

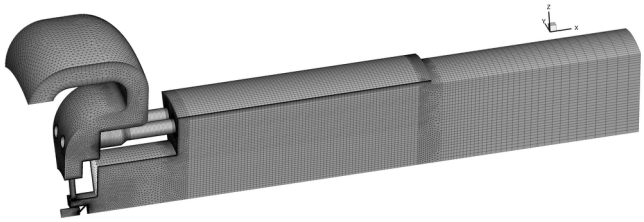

(a) standard, 1 037 815 cells, 458 472 points

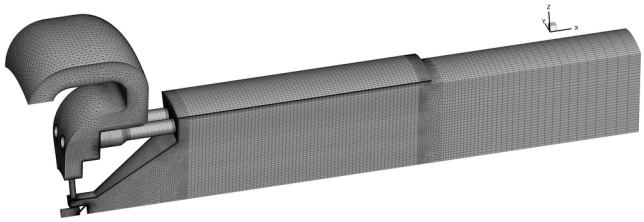

(b) cone, 1 162 935 cells, 494 240 points

Fig. 6: Grid of the 36° wedge of the standard (a) and cone (b) simulated domain.

Pilot Stage Only Operation

The main task of the pilot stage is to allow a cold start of the combustion system as well as stabilize the combustion in lean (e.g. part-load) operating points by feeding hot exhaust gases and radicals to the fuel air mixture of the main stage. During the pilot stage only operation of the combustor, no fuel is supplied to the main fuel nozzles. The combustion air is supplied through one single air inlet. Hence, the air flow runs through both, the main and the pilot stage as seen in Fig. 3. Therefore there is a strong influence on the combustion behavior on the pilot stage due to the large IRZ caused by the high momentum jets at an air inlet temperature of 650°C.

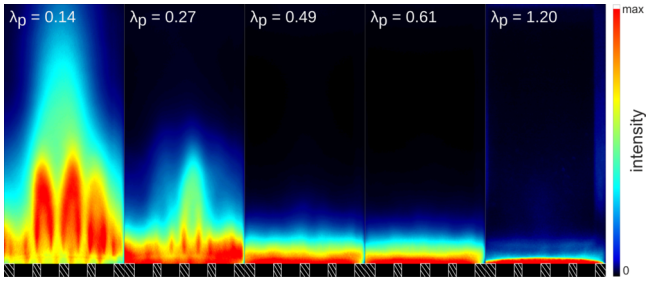

(a) standard

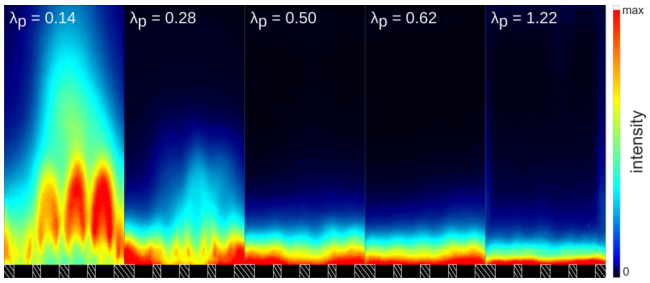

(b) cone

Fig. 7: OH* chemiluminescence for five different air numbers λ_p of the pilot stage at $\dot{m}_{air}$ = 60 g/s for the standard and the cone combustor.

Figure 7 shows a series of five OH* chemiluminescence (OH-CL) images for the standard (Fig. 7a) and the cone (Fig. 7b) combustor. The fuel mass flow rate is decreasing from left to right, with the lowest pilot air number $\lambda_p = 0.14$ corresponding

to a global air number of λ_g = 2.0. Since the pilot dome is not optical accessible, only reactions that reach out into the primary reaction zone (PRZ) are visible. With an increasing fuel mass flow rate and decreasing λ_p, the flame area reaches further into the PRZ and a cone-like reaction zone evolves for $\lambda_p < 0.3$. The excess fuel fed to the pilot stage reacts with the air flow through the main stage, where the single jets become clearly visible. For an air number of $\lambda_p \sim 1.2$, the visible reaction is more apparent for the cone combustor. At lower pilot air numbers, the intensity at the two central nozzles is less for the cone combustor. A reason for this might be a shift in the angular position, where the flow from the pilot fuel nozzle reaches the main air nozzles due to the geometry change.

The NO_x emissions for the pilot stage variation are shown in Fig. 8. The maximum NO_x emissions are seen at $\lambda_p = 0.14$. When reducing the fuel mass flow rate, NO_x emissions decrease to a minimum at a pilot air number of $\lambda_p \sim 0.3$. Schwärzle et al. [2] compared the operation of the combustor in this point to the RQL (Rich-Quench-Lean) combustion principle, where the combustion within the pilot dome is rich. Then the pilot exhaust mixes rapidly with the fresh air from the main stage and the recirculating air from the inner recirculation zone (IRZ), where the remaining fuel is burned under lean conditions. This minimum in NO_x emissions at $\lambda_p \sim 0.3$ is more pronounced for the standard combustor. Following the RQL idea, the local maximum in NO_x emissions should be at λ_p close to unity. As indicated by the green arrow, the local maximum in NO_x emission shifts from $\lambda_p = 0.61$ for the standard to $\lambda_p = 0.83$ for the cone combustor, while remaining at the same emission level. In [2] it was assumed, that the shift in local maximum to a lower pilot air number is a result of the inner recirulation zone (IRZ). Given that the IRZ has not changed significantly, the ORZ may have an influence on the local equivalence ratio within the pilot stage, too. This is also indicated by the lean operating point for the pilot stage only operation. For the standard combustor, the flame extinguishes for $\lambda_p > 1.2$, while for the cone combustor, the flame is still stable up to λ_p = 1.6.

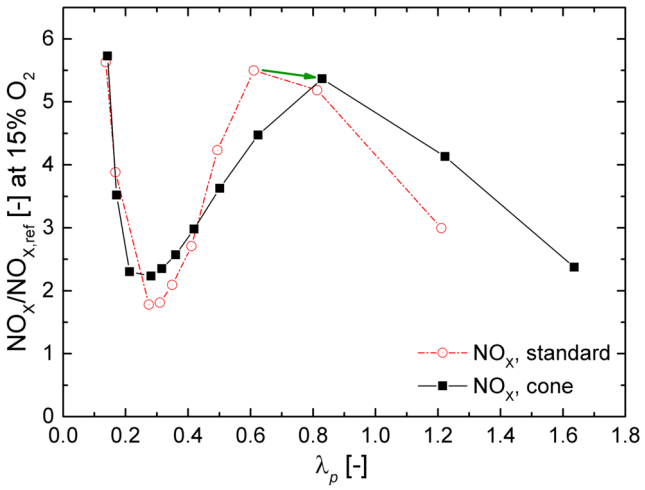

Fig. 8: Normalized NO_x emissions versus λ_p at $\dot{m}_{air}$ = 60 g/s for the standard and the cone combustor.

The shape of the CO emissions in Fig. 9 are almost identical for both combustor designs. From the minimum at λ_p = 0.2, there is a strong increase in CO emissions up to λ_p = 0.5 with a further decrease in fuel mass flow rate. At this point, the largest amount of the fuel fed to the pilot stage enters the PRZ, but the local equivalence ratio is too low for flame stabilization. For $\lambda_p > 0.5$, CO emissions are higher for the cone combustor, whereas its operating range is also extended to higher pilot air numbers. The emission level at the last stable operating point for both combustors is similar.

The influence of the design modification is rather low on the emission level for the pilot stage only operation. The shift in the local maximum of the NO_x emissions indicates local equivalence ratio changes due to the missing ORZ.

Main Stage Only Operation

Figure 10 shows the OH-CL images of the main stage air number variation from λ_m = 1.9 to 3.3. With an increasing air number, the flames become less discrete and move further away from the burner exit plane. At same air number, the images from the cone combustor look less discrete than for the standard combustor. Reasons for this might be a reduction in the peak signal intensity or a more global reduction in signal intensity. This can be the result of a lower OH-CL concentration caused by a leaner or colder reaction zone due to a possibly better mixing of the recirculated exhaust and the cold pilot air flow rate with the fresh fuel air mixture of the main stage for the cone combustor. About 6-7% of the total air stream is fed to the flame through the air swirler of the pilot stage.

The original publication is available at http://dx.doi.org/10.1115/1.4037749

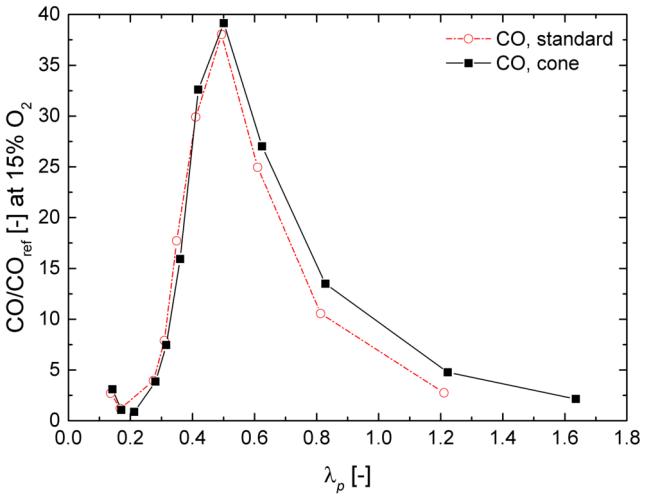

Fig. 9: Normalized CO emissions versus λ_p at $\dot{m}_{air}$ = 60 g/s for the standard and the cone combustor.

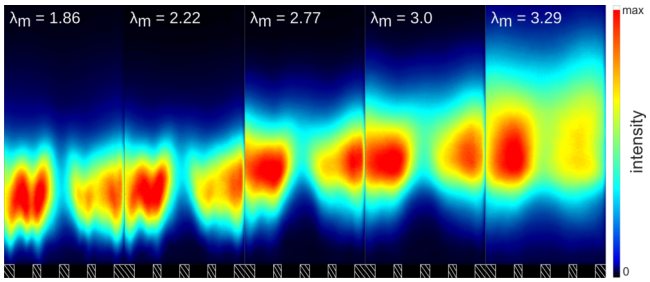

(a) standard

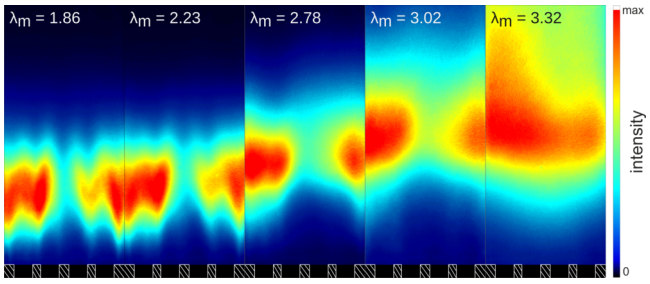

(b) cone

Fig. 10: OH* chemiluminescence for five different air numbers λ_m of the main stage at $\dot{m}_{air}$ = 60 g/s for the standard and the cone combustor.

The flame shape can be described in more detail using Fig. 11, where the flame length (FL) and height above the burner (HAB) are given for the main stage only operation. With an increasing air number the HAB is increasing for both geometries. The sudden drop in HAB for the cone combustor at the last stable operating point λ_m = 3.3 is an indicator of a lean blowout (LBO). The flame length for the standard combustor decreases up to a minimum at λ_m = 2.8, followed by a steep rise when the flame approaches the LBO. For a main stage air number $\lambda_m > 2.4$, the FL is higher for the cone combustor.

The NO_x emissions for the main stage only operation are shown in Fig. 12. For an increase in air number, NO_x emissions are decreasing. The NO_x emissions for the cone combustor are approximately 50% lower than for the standard combustor for all operating points. This indicates, that the mixing of the recirculated air stream with the fuel air mixture from the main stage is more thoroughly with a cone shaped pilot stage.

The CO and UHC emissions in Fig. 13 give a similar expression. With an increasing air number, CO emissions are decreasing. At the onset of unstable combustion for $\lambda_m > 2.6$, CO emissions begin to rise with UHC emissions following in accordance. For air numbers $\lambda_m < 2.6$, the CO emissions are lower for the cone combustor, followed by an earlier rise in CO and UHC emissions and a lower LBO.

The main stage is significantly influenced by the change in geometry. The new pilot shape as well as the increased pilot

The original publication is available at http://dx.doi.org/10.1115/1.4037749

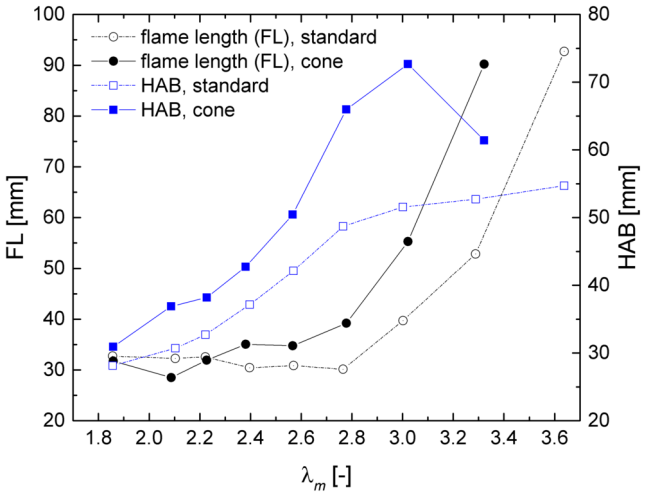

Fig. 11: Flame length (FL) and height above burner (HAB) versus λ_m at $\dot{m}_{air}$ = 60 g/s for the standard and cone combustor.

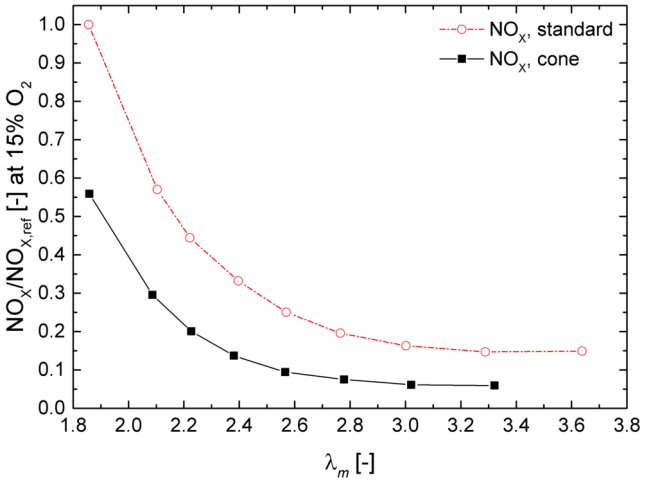

Fig. 12: Normalized NO_x emissions versus λ_m at $\dot{m}_{air}$ = 60 g/s for the standard and cone combustor.

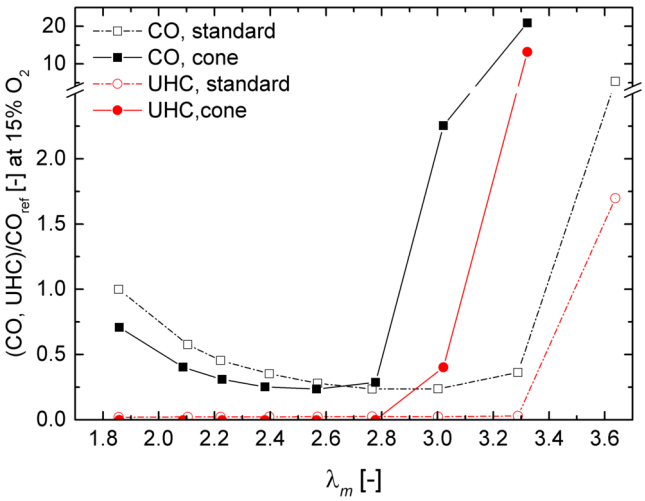

Fig. 13: Normalized CO und UHC emissions versus λ_m at $\dot{m}_{air}$ = 60 g/s for the standard and the cone combustor.

exit diameter seem to improve the mixing of the recirculated air stream as well as the pilot exhaust with the fresh gases fed

to the main stage considerably.

Fuel Split Variation

Figure 14 shows the OH-CL images of the fuel split variation for both geometries. The fuel split is decreasing from right (only main stage operation) to left (only pilot stage operation), which leads to a decrease in HAB. The FL is approximately constant from S_f = 1 to 0.83. For an increasing pilot fuel mass flow rate, the FL increases and the cone-like flame shape appears for $S_f < 0.7$.

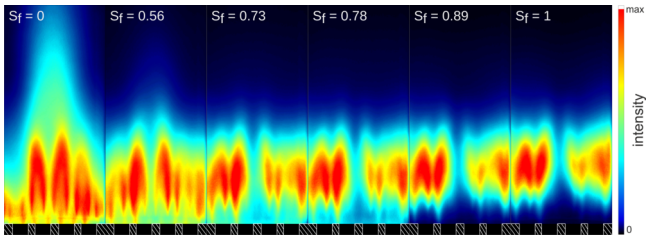

(a) standard

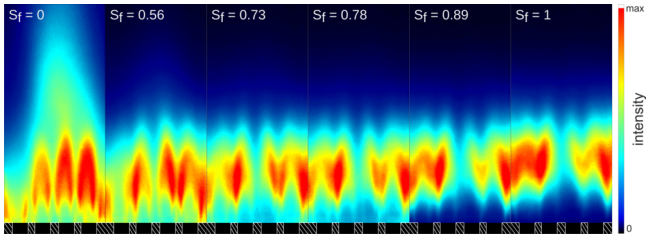

(b) cone

Fig. 14: OH-CL for a fuel split variation from $S_f = 0$ (only pilot stage) to 1 (only main stage) at a global air number $\lambda_g = 2.0$ and $\dot{m}_{air}$ = 60 g/s for the standard and the cone combustor.

In order to compare the split variation to the results from the separated operation of the two stages, all emissions are given on a wet basis without the correction for oxygen content. Figure 15 shows the NO_x emissions plotted against the fuel split S_f. For the pilot and main stage only operation, the fuel split is only a theoretical value, since no fuel was run through the respective other stage. The fuel mass flow rates are given on the top horizontal in order to facilitate the understanding of the graph. The fuel mass flow rate fed to the main stage (MS) is given in blue, while the fuel mass flow rate that is fed to the pilot stage (PS) is given in red. There are cases, where the curve of the pilot stage and the main stage, respectively, have measurement points at the same fuel split. For these points, the sum of both given fuel mass flow rates equals the total fuel mass flow rate of the split variation, which is $\dot{m}_f$ =1.8 g/s. The main stage NO_x emissions show no influence due to the uncorrected emission values. Within the pilot stage only operation, the local maximum is less distinctive for the standard combustor in comparison to Fig. 8, while it is no longer apparent for the cone combustor. The NO_x emissions for the split variation increase for a decreasing fuel split. The local maximum in NO_x emissions from the pilot stage at S_f = 0.78 can be seen in the split variation of the standard combustor. Throughout the whole split variation, the NO_x emissions of the cone combustor are lower than for the standard combustor.

Figure 16 shows the CO emissions (wet) for the split variation, as well as the pilot and main stage only operation. The fuel mass flow rates of the pilot and the main stage are given on the top horizontal axis. For the pilot stage only operation, there is no visible influence of the changed geometry. The CO emissions for the fuel split variation are decreasing when reducing the fuel split from S_f = 1.0 to 0.9. With a further increase in pilot fuel mass flow rate, CO emissions start to rise. Throughout the whole variation, CO emissions are considerably lower for the cone combustor.

Simulated Fuel Split Variation

Reactive simulations were carried out at a fuel split of S_f = 0.93 and 0.78, respectively. In Tab. 2, the relative pressure losses (Eqn. (2)) calculated from the simulations are compared to the measured pressure losses from the experiment. For the simulation, the static pressure at the outlet of the domain was regarded as ambient pressure. The simulated results show a very good agreement with the measurements, which indicates a good representation of the actual flow field.

The original publication is available at http://dx.doi.org/10.1115/1.4037749

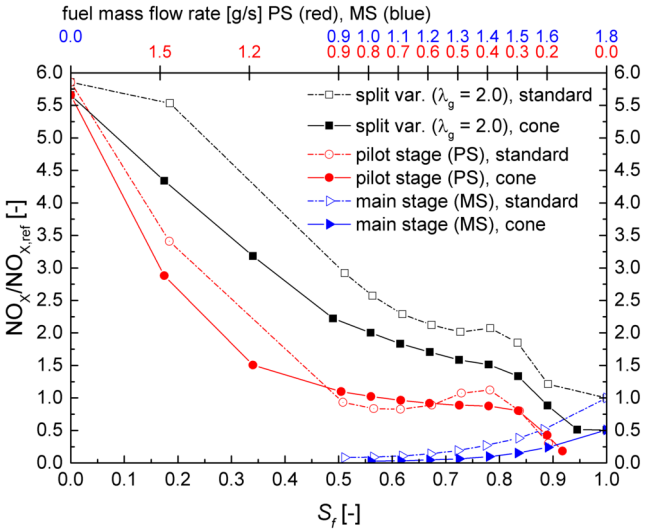

Fig. 15: Normalized, uncorrected NO_x emissions versus (theoretical) fuel split for pilot only, main only and combined operation for the standard and the cone combustor.

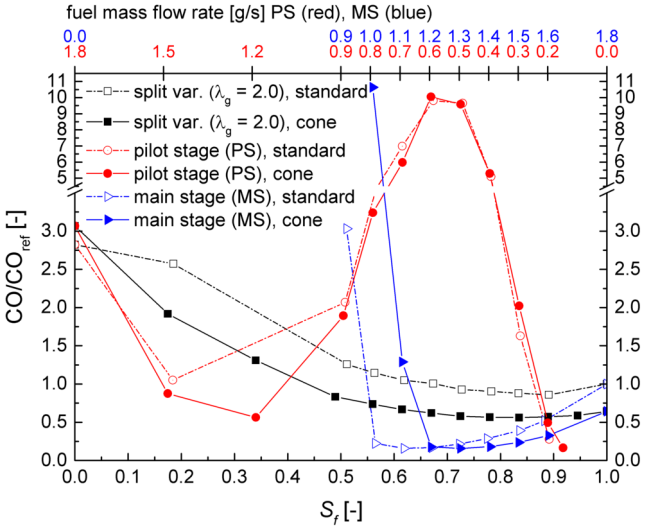

Fig. 16: Normalized, uncorrected CO and UHC emissions versus (theoretical) fuel split for pilot only, main only and combined operation for the standard and the cone combustor.

The mixing quality at the exit plane of the technically premixed main stage can be described using the coefficient of variation (*COV*) [19] wich was evaluated for the CH_4 mole fraction. For the cone and the standard combustor, the *COV* is 0.9 and 0.5, respectively. Therefore, the mixing quality of the main stage at the combustor exit plane is better for the standard combustor. This emphasizes the positive effect of the conical pilot stage on the mixing within the combustion chamber.

In order to evaluate the influence of the changes in the IRZ as seen from the absolute velocity distribution and streamline plot in Fig. 3, the recirculation rate

$$R = \frac{\dot{m}_{recirc}}{\dot{m}_f + \dot{m}_{air}} \tag{5}$$

was calculated for the axial locations -0.05 < x < 0.3, where the combustor exit plane corresponds to x = 0. Figure 17 shows the axial distribution of the recirculation rate *R* for the non-reactive and reactive flow fields of the standard and the cone combustor. For the non-reactive flow field, the recirculation rate is much higher than for the reactive flow field and reaches almost unity for the standard combustor. This means that the amount of recirculated exhaust gas almost equals the amount of fresh fuel and air fed to the combustor. While the area that is occupied by the recirculated flow is larger for the

The original publication is available at http://dx.doi.org/10.1115/1.4037749

Table 2: Relative (static) pressure loss in [%]in simulation (sim) and experiment (exp).

#	Description	$\Delta p_{rel,sim}$	$\Delta p_{rel,exp}$
1	std	2.30	
2	std, comb.	2.40	2.22
3	std, comb.	2.37	2.17
4	cone	2.29	
5	cone, comb.	2.40	2.37
6	cone, comb.	2.36	2.33

cone combustor, the maximum recirculation rate is decreasing at same boundary conditions. Though, the mass flow rate that is recirculated into the pilot stage is increased for the cone combustor. Differences on the flow field between the different operating points at $S_f = 0.93$ and 0.78 are small.

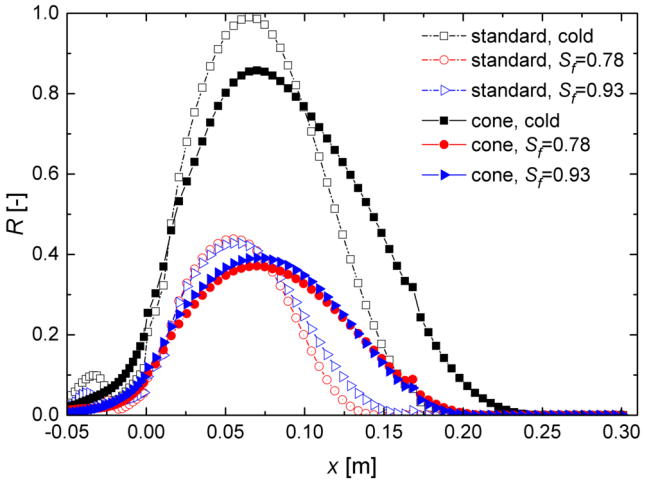

Fig. 17: Recirculation rate R along the axial location x for the reactive and non-reactive numerical simulations of the standard and cone combustor.

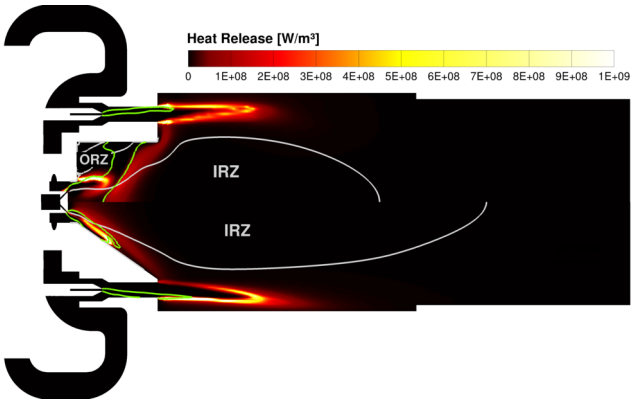

Fig. 18: CFD simulation of the standard (top) and cone (bottom) combustor in the atmospheric test rig at $\dot{m}_{air} = 60$ g/s a fuel split of $S_f = 0.78$ and 650 °C, showing the averaged heat release rate. The green isoline indicates the local air number $\lambda = 2$. The white isoline indicates an axial velocity of u = 0.

Figure 18 shows the heat release rate and isolines at local air number $\lambda = 2.0$ (green) and axial velocity u = 0 m/s (white) for the simulation at $S_f = 0.78$, which corresponds to the local maximum in NO_x emissions of the fuel split variation. For the cone combustor, one reaction zone is apparent within the pilot stage. The isoline that indicates zero axial velocity runs through the reaction zone. This implies, that the recirculated mass flow rate directly takes part in the pilot stage combustion and flame stabilization. This confirms the theory that the local maximum in NO_x emissions for the pilot stage operation is shifted to lower pilot air numbers due to the influence of the IRZ. Within the pilot stage of the standard combustor, two separated reaction zones are apparent, that are separated by the isoline of the local air number. Here it becomes obvious, that the IRZ and the ORZ form two separated reaction zones. The reaction zone originating from the ORZ is most likely responsible for the local maximum in NO_x emissions in Fig. 15. At the main stage nozzle, the fuel flow is deflected to the outer radial edge of the nozzle exit. The reaction zone of the pilot stage for both combustors extends up to the reaction zone of the main stage. Therefore, the reactions at the main stage are stabilized directly at the burner exit plane.

The heat release at a fuel split of $S_f = 0.93$ is shown in Fig. 19. The isolines in green and white correspond to a local air number of $\lambda = 2.0$ and an axial velocity of u = 0 m/s, respectively. The reaction zone in the pilot stage looks similar for the two combustor designs. Since the reaction zone does not extend up to the main stage, the flame of the main stage is most likely only stabilized due to the hot exhaust gases of the pilot stage. As a result, the flame of the main stage does not stabilize at the inner edge of the main nozzle as for the simulation at $S_f = 0.78$. Similar to the results at $S_f = 0.78$, the fuel flow is deflected to the outer edge of the main nozzle. This deflection is stronger for the cone combustor which is the reason for its lower mixing quality at the combustor exit plane. The flame stabilization takes place at this location.

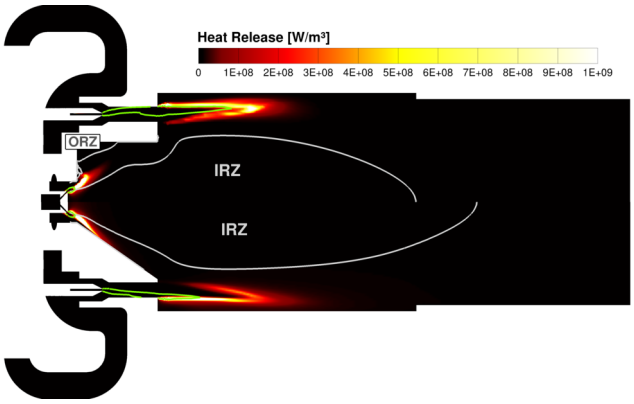

Fig. 19: CFD simulation of the standard (top) and cone (bottom) combustor in the atmospheric test rig at $\dot{m}_{air} = 60$ g/s a fuel split of $S_f = 0.93$ and 650 °C, showing the averaged heat release rate. The green isoline indicates the local air number $\lambda = 2$. The white isoline indicates an axial velocity of u = 0.

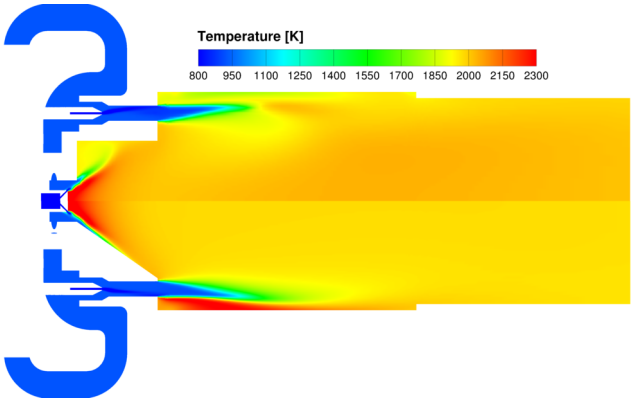

Fig. 20: CFD simulation of the standard (top) and cone (bottom) combustor in the atmospheric test rig at $\dot{m}_{air} = 60$ g/s a fuel split of $S_f = 0.93$ and 650 °C, showing the averaged temperature.

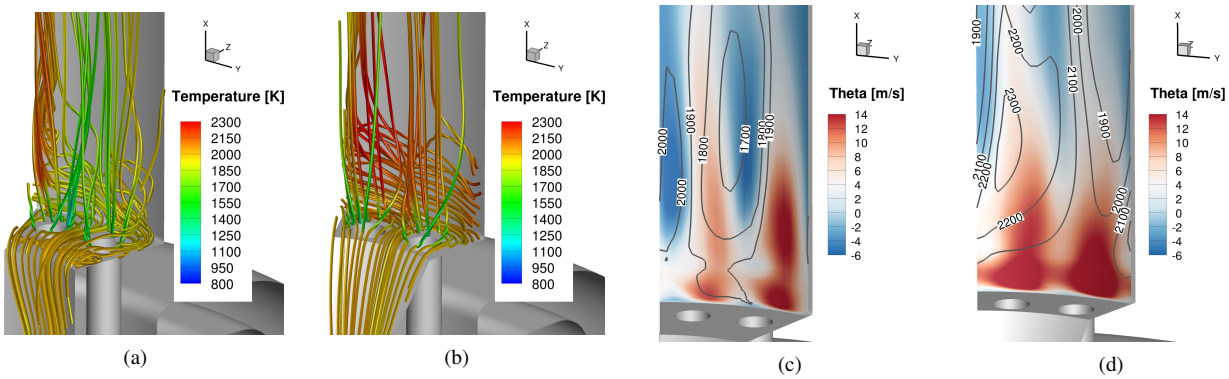

Fig. 21: CFD simulation of the standard (a,c) and cone (b,d) combustor in the atmospheric test rig at $\dot{m}_{air} = 60$ g/s a fuel split of $S_f = 0.78$ and 650 °C. (a,b) show streamlines colored by averaged temperature. (c,d) show an isosurface of constant radius close to the outer wall colored by the circumferential velocity θ and isolines of constant averaged temperature.

Figure 20 shows the temperature distribution within both combustors for a fuel split of $S_f = 0.93$. The temperature distribution within the recirculation zone of both combustors and at the exit plane is quite uniform. The highest temperatures occur directly at the pilot fuel nozzle at the IRZ. The temperature within the ORZ of the standard combustor is below the combustor exit temperature, hence the influence on NO_x emissions of the ORZ is presumably low. At the outer edge of the main nozzle, temperatures are much higher for the cone combustor than for the standard combustor. In order to evaluate this phenomenon, streamline plots for the standard and the cone combustor are given in Figs. 21a and b. In the standard combustor, the flow from the pilot stage is redirected by 90 degree, where a small recirculation zone is formed at the inner edge of the main nozzles, before it mixes with the main stage flow. The temperature of the streamlines at the inner edge of the main nozzles are higher than at the outer edge. For the cone combustor, the pilot exhaust is fed to the main stage nozzles more uniform. At the outer edge of the main nozzles, the flow is directed in the circumferential direction as an effect of the pilot swirl. For the cone combustor, the temperature of the streamlines is increased compared to the inner edge.

The differences in circumferential velocity θ and in the temperature distribution close to the combustion chamber wall is visualized in Figs. 21c and d. For the cone combustor, a steady circumferential flow with velocities above 10 m/s exists at the outer edge of the main nozzles. This recirculation zone is most likely the reason for the increased temperature, which is indicated by the isolines, in this area. In the standard combustor, the flow in the circumferential direction is much less pronounced and the temperature is 200-300 K lower than for the cone combustor.

Air Number Variation at Constant Thermal Load

A global air number variation at a thermal load was carried out for $\dot{Q} = 100$ kW at a constant fuel split of $S_f = 0.93$. These results are useful in order to determine the optimal air split between combustor and dilution air for the MGT combustion system. This air split usually is not controlled for a MGT. Hence, for the design of the dilution air holes, the whole operating range of the MGT has to be taken into account. The global air number at part load is therefore higher than the global air number at full load conditions.

Figure 22 shows the OH-CL images for the global air number variation for the standard and the cone combustor. Similar to the results from the main stage only operation, the flames are more discrete and elongated for a global air number $\lambda_g \leq 2$. For air numbers above $\lambda_g = 2$, the flames become less discrete until only one single reaction zone is visible. The reaction zone for the cone combustor is less discrete in comparison to the standard combustor for $\lambda_g < 2.6$. For higher air numbers, the influence of the pilot stage is more pronounced for the cone combustor and the flame stabilization is enhanced. A reason for this might be the formation of a circumferential recirculation zone as mentioned in the previous section. This recirculation helps stabilizing the combustion at lean conditions.

Figure 23 shows the NO_x, CO and UHC emissions for the global air number variation at constant thermal load. For an increasing air number, both CO and NO_x emissions decrease to a minimum at $\lambda_g = \sim 2.6$, which would be the optimum air number for the current thermal load and preheat temperature. Due to the geometry modification, emission levels are reduced in comparison the the standard combustor.

Summary and Conclusion

In this study, a geometry variation of the design of a jet-stabilized combustor was experimentally and numerically analyzed in detail and compared to the standard design [2]. The experiments were carried out on an atmospheric test rig. The

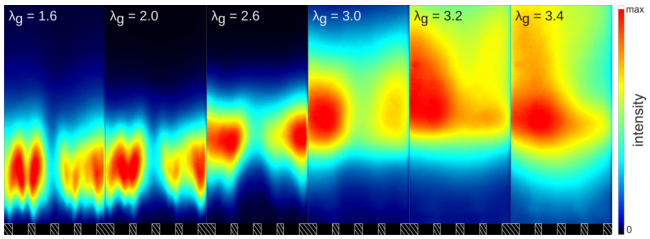

(a) standard

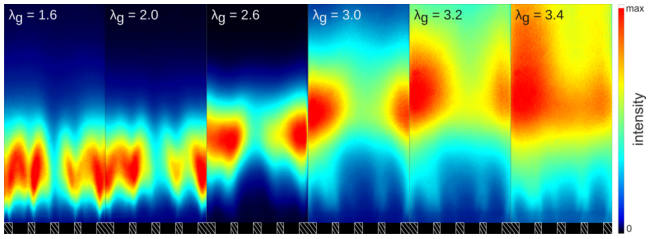

(b) cone

Fig. 22: OH-CL for a global air number variation λ_g at a thermal load of Q_{th} = 100 kW and constant fuel split S_f = 0.93 for the standard and the cone combustor.

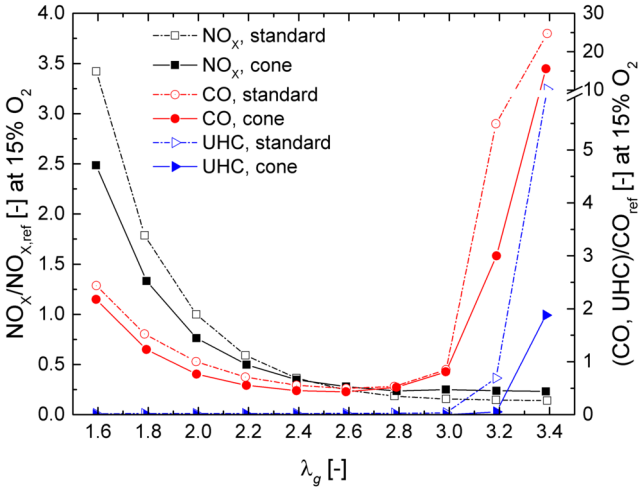

Fig. 23: Normalized NO_x, CO and UHC emissions versus global air number for the standard and the cone combustor.

flames were analyzed using OH^* chemiluminescence and emission measurements were carried out. The numerical simulation gave valuable insights in the flow physics and reaction zones as well as the temperature distribution. This supplementary data played a key role for the understanding of the experimental results.

The introduction of a cone-shaped pilot stage was a first step to the optimization of the pilot stage emissions with the goal of removing the outer recirculation zone (ORZ). With the simulations it could be shown, that the ORZ was the reason for the local maximum in NO_x emissions at a fuel split of S_f = 0.78. The inner recirculation zone had a direct effect on the combustion in the pilot stage, since the recirculation directly interacted with the pilot stage reaction zone. Although the geometry modification had little effect on the pilot stage emissions, both the CO and NO_x emissions of the main stage or primary reaction zone could be reduced substantially. This was due to a better mixing of recirculated exhaust gases with the fresh fuel air mixture from the main stage. In addition, the combustion within the main stage was better stabilized by the pilot stage due to a circumferential recirculation zone at the combustor liner, where the temperature was increased. Overall, the modified geometry is advantageous for the combustion system in terms of emissions and flame stabilization.

Outlook

The pilot stage of the combustion system works basically as a supply of hot exhaust gases for the main stage. For a re-design of the combustor stages, a better pre-mixing of pilot air and fuel prior to combustion would be advantageous

concerning the pilot stage emissions. A reduction of the interference of the main stage with the pilot stage would be preferable in order to optimize the pilot stage combustion more independently. An example for a rich pilot lean (RPL) combustion is the Siemens SGT-750 dry low NO_x (DLN) burner [20]. The optimization potential within the main stage is due to the deflection of the fuel flow to the outer edge of the main nozzles, where the flame easily stabilizes. By optimizing the flow within the main mixing section and optimizing the premixing quality, emissions could be reduced further.

Additional laser measurements like PIV (Particle Image Velocimetry) or LIF (Laser Induced Fluorescence) would allow a better validation of the numerical results. For a more detailed analysis of the combustor, the application of scale resolving simulations [21] and a more detailed reaction mechanism including NO_x reactions would be desirable.

References

[1] Zanger, J., Monz, T., and Aigner, M., 2015. "Experimental Investigation of the Combustion Characteristics of a Double-Staged FLOX-Based Combustor on an Atmospheric and a Micro Gas Turbine Test Rig". In ASME Pap. No. GT2015-42313.

[2] Schwärzle, A., Monz, T., and Aigner, M., 2016. "Detailed Examination of Two-Staged Micro Gas Turbine Combustor". In ASME Pap. No. GT2016-57730.

[3] Kazakov, A., and Frenklach, M. Drm22. http://www.me.berkeley.edu/drm/.

[4] IEA, 2016. Key worl energy trends – excerpt from: World energy balances. Online.

[5] Monz, T., Stöhr, M., O'Loughlin, W., Zanger, J., Hohloch, M., and Aigner, M., 2015. "Experimental Investigation of the Combustion Characteristics of a Double-Staged FLOX-Based Combustor on an Atmospheric and a Micro Gas Turbine Test Rig". In ASME Pap. No. GT2015-42387.

[6] Zanger, J., Monz, T., and Aigner, M., 2013. "Experimental Investigation of the Influence of Combustor Cooling on the Characteristics of a FLOX-based Micro Gas Turbine Combustor". *Prog. Gas Turbine Perform.*, pp. 165–184.

[7] Schütz, H., Lückerath, R., Kretschmer, T., Noll, B., and Aigner, M., 2008. "Analysis of the Pollutant Formation in the FLOX Combustion". *J. Eng. Gas Turbines Power,* **130**(1), Jan., p. 11503.

[8] Lückerath, R., Meier, W., and Aigner, M., 2008. "FLOX Combustion at High Pressure With Different Fuel Compositions". *J. Eng. Gas Turbines Power,* **130**(1), Jan., p. 11505.

[9] Flamme, M., 2001. "Low NOx Combustion Technologies for High Temperature Applications". *Energy Convers. Manag.,* **42**(15-17), Oct., pp. 1919–1935.

[10] Lammel, O., Stöhr, M., Kutne, P., Dem, C., Meier, W., Aigner, M., and St, M., 2011. "Experimental Analysis of Confined Jet Flames by Laser Measurement Techniques". In ASME Pap. No. GT2011-45111.

[11] Dandy, D. S., and Vosen, S. R., 1992. "Numerical and Experimental Studies of Hydroxyl Radical Chemiluminescence in Methane-Air Flames". *Combust. Sci. Technol.,* **82**(1-6), pp. 131–150.

[12] Bundesministerium für Umwelt Naturschutz und Reaktorsicherheit, 2002. Erste Allgemeine Verwaltungsvorschrift zum Bundesimmissionsschutzgesetz (Technische Anleitung zur Reinhaltung der Luft, TA Luft).

[13] Di Domenico, M., 2008. "Numerical Simulation of Soot Formation in Turbulent Flows". PhD thesis, Institute of Combustion Technology of Aerospace Engineering, University of Stuttgart.

[14] Menter, F. R., 2009. "Review of the shear-stress transport turbulence model experience from an industrial perspective". *International Journal of Computational Fluid Dynamics,* **23**(4), pp. 305–316.

[15] Gerlinger, P. and Noll, B. and Aigner, M., 2005. "Assumed PDF modelling and PDF structure investigation using finite-rate chemistry". *Progress in Computational Fluid Dynamics, An International Journal,* **5**(6).

[16] Girimaji, S. S., 1991. "Assumed Beta-PDF Model for Turbulent Mixing: Validation and Extension to Multiple Scalar Mixing". *Combustion Science and Technology,* **78**, pp. 177 – 196.

[17] Frenklach, M., Wang, H., Yu, C.-L., Goldenberg, M., Bowman, C., Hanson, R., Davidson, D., Chang, E., Smith, G., Golden, D., Gardiner, W., and Lissianski, V. Gri-mech 1.2. http://www.me.berkeley.edu/gri_mech/.

[18] Zanger, J., 2016. "Experimentelle Charakterisierung eines atmosphärisch betriebenen, FLOX-basierten Mikrogasturbinenbrenners für Erdgas". Dissertation, Universität Stuttgart.

[19] Shamloo, A., Madadelahi, M., and Akbari, A., 2016. "Numerical simulation of centrifugal serpentine micromixers and analyzing mixing quality parameters". *Chemical Engineering and Processing: Process Intensification,* **104**, pp. 243 – 252.

[20] Kundu, A., Klingmann, J., Subash, A. A., and Collin, R., 2016. "Pilot-Pilot Interaction Effects on a Prototype DLE Gas Turbine Burner Combustion". In ASME Pap. No. GT2016-57338.

[21] Menter, F. R., and Egorov, Y., 2006. "SAS Turbulence Modeling of Technical Flows". *Direct and Large-Eddy Simulation V, Part XV*, pp. 687–694.